Analogue modelling of the Ainsa oblique zone in the Southern Central Pyrenees, Spain

Journal Article

Author(s):
van der Werf, Iris; Schellart, Wouter P.; Strak, Vincent; van Agtmaal, Luuk (iD); Blankendal, Ruiz
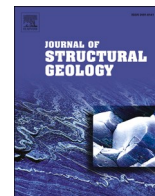
Analogue modelling of the Ainsa oblique zone in the Southern Central Pyrenees, Spain

Iris van der Werf [a],[*], Wouter P. Schellart [a], Vincent Strak [a],[b], Luuk van Agtmaal [c], Ruiz Blankendal [a]

[a] *Department of Earth Sciences, Vrije Universiteit Amsterdam, De Boelelaan, 1105HV, Amsterdam, Netherlands*
[b] *Aix-Marseille University, CEREGE, CNRS, IRD, INRAE, Aix-en-Provence, France*
[c] *Geophysical Fluid Dynamics Group, Department of Earth Sciences, ETH Zürich, Switzerland*

ARTICLE INFO

ABSTRACT

The Pyrenees are a collisional orogen striking WNW-ESE. However, in the Ainsa oblique zone in the south-central part of the Pyrenees, faults and folds rotate to ~N–S over a westward thinning evaporitic layer. The influence of lateral change in basal friction due to declining evaporitic layer thickness in a fold-and-thrust belt is studied by analogue modelling simulating the Ainsa oblique zone. In the experiments the transition zone is simulated by a viscous silicone mixture sheet that laterally changes in thickness adjacent to frictional-plastic quartz-sand. The models confirm that a transition between weak and strong basal friction causes oblique structures to develop. Weak detachment zones are prone to fault propagation whereas strong detachment zones are prone to imbrication. At the transition zone those structural styles are combined, resulting in a complex domain. The differences in deformation style cause dextral shear and clockwise rotation in the transition zone and larger horizontal deformation propagation in the weak basal friction zone. Structures produced in the analogue models are compared to structures in the Ainsa oblique zone and found to be representative. Therefore, this study shows that transition between weak and strong detachment layers can explain the regional structural deformation style in the Ainsa oblique zone.

1. Introduction

Collisional mountain belts generally form due to the collision of two continents, and well-known examples on Earth include the Alps, Pyrenees, Caucasus, Zagros and Himalaya. The Pyrenees are a continent-continent collisional orogen located between France and Spain that formed due to the convergence of the Iberian peninsula microplate and the Eurasian plate during the Cretaceous to early-middle Miocene (Fitzgerald et al., 1999; Vergés et al., 2002). The greatest amount of shortening has been recorded in the eastern Pyrenees, 145–165 km (Muñoz, 1992; Fitzgerald et al., 1999; Beaumont et al., 2000). Towards the west, the amount of shortening decreases and reaches an average of 80 km (Alonso et al., 1996; Teixell, 1998; Muñoz et al., 2013). In this WNW-ESE striking, elongated mountain range the folds and thrusts generally have a similar strike. In the southern Central Pyrenees, however, the fold-and-thrust belt is strongly curved and in places folds and thrusts strike at high angle (~60–90°) to the main strike of the orogen (Fig. 1; Muñoz, 1992; Fitzgerald et al., 1999; Muñoz et al., 2013,

Chanvry et al., 2018). Curvatures are common in fold-and-thrust belts and have been recognized as important features for understanding orogens, even before the theory of continental drift by Alfred Wegener was widely accepted (Suess, 1909; Hobbs, 1914). More recent studies agree that curvatures in orogens can develop as primary, progressive or secondary curvatures, depending on their kinematics (Marshak, 2004; Weil and Sussman, 2004; Muñoz et al., 2013). Primary curved thrust belts form initially during deformation due to inversion of pre-existing faults and basins with a different orientation than the shortening direction. Typically, no vertical axis rotation is involved in primary curved orogens. In contrast, both progressive and secondary curved belts are influenced by vertical axis rotations caused by shearing, respectively during and after initial deformation (Marshak, 2004; Weil and Sussman, 2004). The curvature in the Pyrenean orogen has been classified as a progressive curvature, which has been attributed to the existence of unevenly distributed Triassic evaporites that form a detachment layer beneath the fold-and-thrust belt (Weil and Sussman, 2004; Soto et al., 2006; Weil et al., 2010; Muñoz et al., 2013). The Triassic evaporites

---

deposited in shallow marine extensional basins during rifting induced by the break-up of Pangea (Vergés et al., 2002; Chanvry et al., 2018).

The Pyrenees are characterised by a high quantity and good quality of outcrops and have been thoroughly studied. These studies have allowed a detailed documentation of the southern Central Pyrenees curved fold-and-thrust belt, including the Ainsa oblique zone, which is located at the western edge of the curved belt (Fig. 1). Despite earlier detailed studies such as Muñoz (1992), Dreyer et al. (1999), Fitzgerald et al. (1999), Vergés et al. (2002) and Muñoz et al. (2013) there is still no general consensus as to what has caused the curved belt, and the Ainsa oblique zone in particular. The Ainsa oblique zone is a zone of folds and thrusts that strike obliquely (~N–S) with respect to the general strike of the folds and thrusts in the Southern Pyrenees and the orientation of the orogen (~WNW-ESE) (Fig. 1). It is located at the western end of the Bóixols, Montsec and Serres Marginals thrust sheets, which reach the surface in the region, and above the westward thinning Triassic evaporites (Vergés et al., 2002; Vidal-Royo et al., 2009; Muñoz et al., 2013). It is therefore suitable for studying the influence of lateral changes in basal friction on the structural evolution of a fold-and-thrust belt (Figs. 1 and 2). This study aims to test the hypothesis that the gradual, lateral (west to east) transition from high to low basal friction in the Ainsa oblique zone influences the regional structural style and causes oblique structures to form due to differences in deformation style between domains overlying a contrasting basal rheology. To address this aim, we present laboratory-based analogue models of fold-and-thrust belt experiments using an upper sand layer and a basal silicone layer with a laterally variable thickness.

For many decades analogue modelling has been used to simulate deformation processes in convergent settings and has thereby enhanced the understanding of fold-and-thrust belts (e.g., Koyi, 1995; Marshak, 2004; Graveleau et al., 2012; Schellart and Strak, 2016). These earlier studies managed to explain many parameters that influence the evolution of fold-and-thrust belts. Mulugeta (1988) showed that different basal rheologies form different deformation styles, imbricated and compact thrust belts for high basal friction, and lower topography and more spaced faults for low basal friction. The amount of basal friction itself controls the structural style of deformation, with rigid in sequence faulting and imbrication caused by high basal friction and fault propagation, and box folding and out of sequence faulting for weak basal friction as endmembers (Mulugeta, 1988; Cassalou et al., 1993; Cotton and Koyi, 2000). Shortening rate is another parameter that influences the geometry of fold-and-thrust belts. Under high shortening rates over a viscous layer fault spacing is close and thrust sheets are short, cover and underlying horse blocks are strongly coupled and underthrusting causes
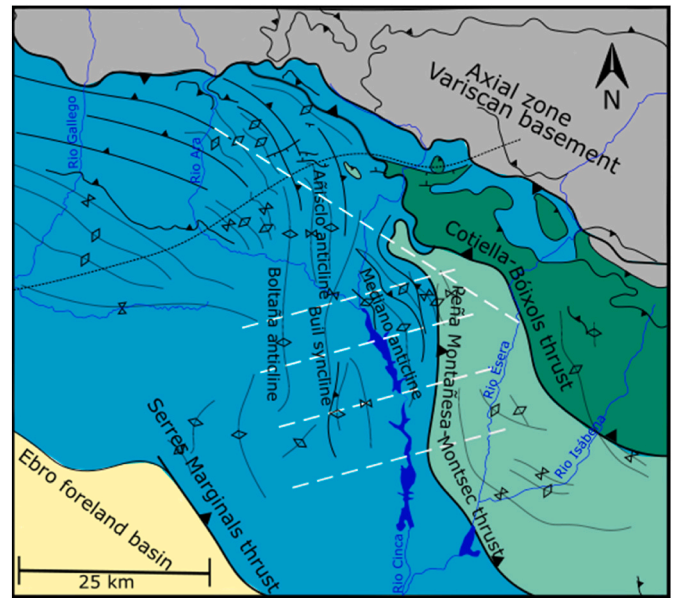

Fig. 2. Schematic structural map of the Ainsa oblique zone. For location see Fig. 1. The white dashed lines show the locations where the slopes are measured for comparison with the experiments. Modified after Muñoz et al. (2013).

a passive roof duplex to develop. Under low shortening rates fault spacing is wide and long thrust sheets develop. Furthermore, decoupling takes place causing cover deformation in front of the horse blocks and the development of an active roof duplex (Couzens-Schultz et al., 2003).

Analogue modelling studies have also been applied to the Pyrenees. For example, Koyi et al. (2004) focused on the process of layer-parallel shortening during convergence and fold-and-thrust belt formation. They applied their analogue modelling results to sedimentary layers from the eastern Spanish Pyrenees fold-and-thrust belt, while Soto et al. (2006) focused on the entire Pyrenees and demonstrated the influence of the backstop on the geometry and structure of the mountain belt. Santolaria et al. (2022) studied the influence of decollement cover thickness in fold-and-thrust belts and demonstrated that a lateral variety in cover thickness triggers differential frontal translation and vertical axis rotation. To date, however, no study has modelled the influence of an unevenly distributed and laterally gradually thinning viscous basal detachment layer adjacent to a brittle basal detachment layer on fold-and-thrust belt evolution. Vidal-Royo et al. (2009) conducted a
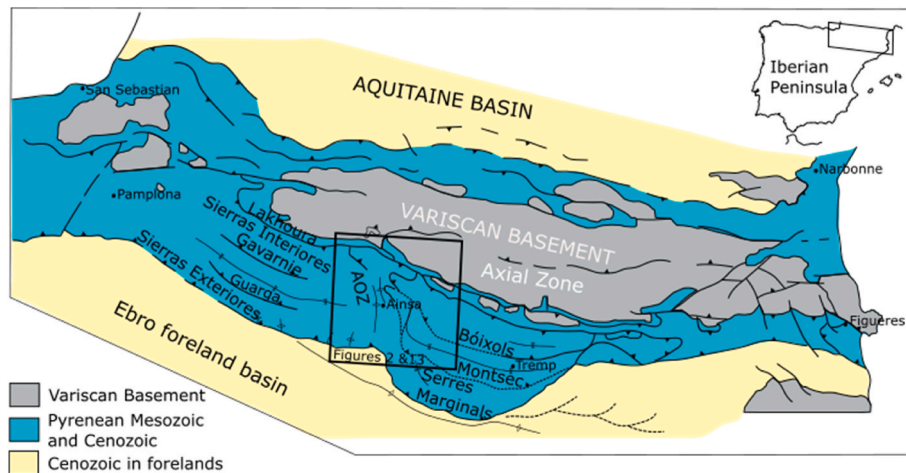

Fig. 1. Structural overview map of the Pyrenean orogen showing the most significant units and structures. Modified after Muñoz et al. (2013). The black square illustrates the outline of the study area. A close-up of the study area can be seen in Fig. 2 and 13. The inset on the top right shows the location of the Pyrenees with respect to the Iberian Peninsula. AOZ–Ainsa Oblique Zone.

study on the thrust geometry as a result of lateral variation in mechanical properties of cover sediments, specifically aimed at the Central Sierras Exteriores (CSE), which are located west and south-west of the study area (Fig. 1). Our approach is comparable to theirs, except that no gradually thinning viscous basal detachment layer was implemented in their study. This study aims to produce an experimental model based on the Ainsa oblique zone that does include a laterally thinning viscous basal detachment layer to explain the curvature and obliquity of the folds and thrusts in the South-Central Pyrenees.

2. Geological setting

The asymmetrical and doubly-wedged WNW-ESE striking Pyrenean fold-and-thrust belt developed from the Late Cretaceous until the Oligocene or early Miocene during collision between the Iberian microplate with the Eurasian plate, following Mesozoic rifting that stopped in the Late Cretaceous (~93 Ma) (Fitzgerald et al., 1999; Vergés et al., 2002; Chanvry et al., 2018). Collision likely started around 83 Ma, when Iberia started converging with Eurasia (Rosenbaum et al., 2002). Partial continental subduction of Iberia underneath the European plate occurred during this collision process (Choukroune et al, 1988; Muñoz et al., 2013). The Pyrenees are generally divided into the Eastern Pyrenees, Central Pyrenees and Western Pyrenees (Fitzgerald et al., 1999; Vergés et al., 2002). Shortening is most pronounced in the Eastern Pyrenees where it reaches an average value of 145–165 km (Muñoz, 1992; Fitzgerald et al., 1999; Beaumont et al., 2000). Towards the west the amount of shortening decreases and reaches an average of 80 km (Alonso et al., 1996; Teixell, 1998; Muñoz et al., 2013). On top of both the Iberian and Eurasian plate thrust systems developed, which are flanked in the north by the Aquitaine foreland basin and in the south by the Ebro foreland basin. In between the northern and southern thrust sheets lies the Axial zone, which is a complex consisting of stacked Variscan basement rocks. The southern thrust sheets formed in a piggyback sequence on the Iberian plate and show three significant southward propagating thrust sheets that have incorporated pre-orogenic and syn-orogenic sediments, including foreland basin sediments (Fitzgerald et al., 1999; Vergés et al., 2002; Muñoz et al., 2013). In the Central Pyrenees, from oldest to youngest and from north to south, these main thrusts are the Cotiella-Bóixols thrust sheet, Peña Montañesa-Montsec thrust sheet and the Sierras Exteriores-Serres Marginals thrust sheet (Fig. 1). In the Western Pyrenees three basement-involved thrust sheets, which are respectively called the Lakhoura, Gavarnie and Guarga thrust sheets are also present (Teixell, 1998). The thrust sheets in the Central Pyrenees developed during Late Cretaceous, Paleocene-Late Ypresian and Lutetian-Oligocene times (Muñoz et al., 2013). The propagation of these thrust sheets is accommodated by the basement thrusts of the axial zone, which are south-vergent and become younger towards the South (Labaume et al., 1985; Teixell, 1998; Muñoz, 1992; Muñoz et al., 2013).

Prior to the Pyrenean orogeny the study area was affected by extension related to the break-up of Pangea. During this extension, laterally discontinuous layers of Triassic (Keuper) evaporitic sediments were unconformably deposited upon the Variscan basement (Vidal-Royo et al., 2009; Muñoz et al., 2013). These evaporites have been covered by Mesozoic and Cenozoic sediments, mostly of marine origin, including limestones and turbidites. The weak evaporites have functioned as a decollement layer for the thrust sheets that have developed in the sedimentary cover sequences of the Southern Pyrenees fold-and-thrust belt (Labaume et al., 1985; Muñoz et al., 2013). Due to the uneven lateral distribution of the basal evaporitic layer there are lateral differences in basal friction, which have affected the deformation style in the Southern Pyrenees on a regional scale.

The Ainsa oblique zone is the study area and consists of a small, ~25 km wide and ~40 km long piggyback basin that originated as a foredeep basin during the early to mid-Eocene. The basin is located south of the axial zone on top of the Gavarnie thrust sheet complex (Fig. 1; Dreyer

et al., 1999; Bakke et al., 2008, Mochales et al., 2012). At first, the sedimentary infill of the Ainsa basin consisted of deep marine sediments and turbidites. Afterwards, during the middle-late Lutetian, collisional events in the region caused uplift and thus a regressive signature in the deposited sediments (Dreyer et al., 1999). After prolonged uplift of the area, alluvial fans dominated the stratigraphy of the Ainsa basin (Muñoz, 1992; Dreyer et al., 1999; Bakke et al., 2008; Mochales et al., 2012). Alluvial fan conglomerates represent the last sedimentary infill of the area (Dreyer et al., 1999). In the central part of the Ainsa oblique zone, the dominant structural orientation is north-south, while to the west and east, the structures curve towards a WNW-ESE orientation, which is the same as the overall strike of the Pyrenees (Fig. 2). The thrusts and folds in the Ainsa oblique zone decouple at the Triassic evaporitic level (Dreyer et al., 1999; Muñoz et al., 2013; Chanvry et al., 2018). This evaporitic detachment layer gradually disappears towards the west within the Ainsa oblique zone. (Fig. 2).

3. Methods

3.1. Experimental set-ups

In this study, analogue experiments have been constructed to model the fold-and-thrust belt evolution in the Ainsa oblique zone of the western part of the Central Pyrenees. The model set-up includes a large rectangular box with a flat base, a vertical moving backstop at the back, fixed side-walls and front wall. The box was filled with either sand or sand and a silicone-iron powder mixture. Two different experimental set-ups were constructed to perform two types of experiments (Fig. 3). The internal lateral dimensions of the model measured 98 cm (along the backstop) and 130 cm (perpendicular to the backstop). The first experimental set-up consisted of a 4 cm thick dry sand layer to test that the set-up was able to reproduce a rectilinear fold-and-thrust belt and to analyse the structures in absence of a viscous detachment layer. For the second experimental set-up, a viscous basal silicone-iron powder layer was introduced to more accurately represent the rheological layering of the sedimentary cover in the Ainsa oblique zone prior to Pyrenean deformation. The set-up consisted of two separately constructed silicone-iron powder layers, the first was a 20 cm wide, 70 cm long, 0–1 cm thick layer that simulated the westward-thinning Triassic Keuper layer in the Ainsa basin. The second was a 35 cm wide, 70 cm long and 1 cm thick sheet that simulated the Keuper layer to the east with a constant thickness (Fig. 3). These two layers were joined during the first phase of construction of the experiment, after which dry sand was sieved on top and surrounding the viscous sheet. During the final phase of construction, cylindric, 10 mm long and 0.5 mm thick black fibres were sprinkled on top of the sand layer to track rotation and displacement during a model run.

3.2. Materials and experimental execution

The viscous Triassic evaporite layer was modelled by a layer of Newtonian viscous polydimethyl-siloxane (PDMS) and iron powder mixture and the overlying brittle Upper Cretaceous to Lutetian lithologies were simulated by a layer consisting of Sibelco quartz sand with a grain size <500 μm. Within the sand, thin coloured marker layers were added to visualise internal deformation structures of the models such as faults in cross-sections. The sand layers were constructed by sieving the sand from a uniform height (20 cm) using a 500 μm sieve. All parameters such as the density contrast between brittle and viscous rheologies, the viscous layer-brittle layer thickness ratio and the width of the basal friction zones in this study were derived from the published literature (Table 1). The experiments containing only sand ran for approximately 45 min at a velocity of 32 cm/h whereas the experiments with both sand and PDMS-iron mixture ran for 24 h at a much slower velocity of 1 cm/h to make sure that the silicone behaved as an approximately linear viscous material. During the sand experiments top view photos were
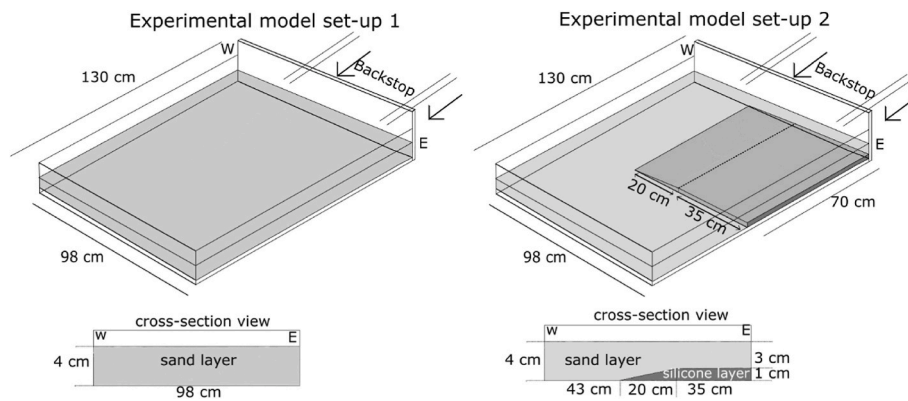
Fig. 3. Schematic 3D perspective view and cross-section view of the two experimental set-ups showing dimensions and the location of viscous and brittle materials. The arrows represent the direction of motion of the backstop. Experiment 4 has used model set-up 1, while experiment 8 (as well as experiment 7 presented in Fig. A1 in the Appendix to test reproducibility) has used model set-up 2.

Table 1
Parameters used for the experimental set-up and to constrain the density contrast between the clastic cover material and the basal viscous material for the natural prototype.

	Material	Density [kg/m³]	Thickness [m]	Viscosity [Pa s]
Nature: sedimentary cover material	Limestones, turbidites, sandstones	2500	2000 (Muñoz et al., 2013)	–
Nature: basal viscous material	Rocksalt	2160	0-400 (Muñoz et al., 2013)	10^{17}-10^{20} (van Keken et al., 1993)
Nature: density contrast		340	–	–
Model: sedimentary cover material	Quartz sand	1590	0.04	–
Model: basal viscous material	Silicone-iron powder mix	1241	0–0.01	6–7 × 10⁴ Pa s
Model: density contrast		349	–	–

taken with an interval of 30 s and during the brittle-viscous experiments every 10 min. At the end of an experimental run, the top surface was covered with a thin layer of coloured loose sand and impregnated with water before cutting cross-sections.

3.3. Scaling and parameters

The experiments are scaled in such a manner that 1 cm in the model represents 500 m in nature (scaling factor: 1: 50,000). The modelled area is 4 cm thick and 98 cm wide and thus represents a natural counterpart of 2 km thickness with a width of roughly 50 km. Our brittle-viscous experiments lasted 24 h, and 1 h in these experiments represents ~0.25 Myr in nature. The Pyrenean orogeny lasted approximately 60 Myr, and the experiments represent some 10% of this duration. The quartz sand used during the experiments had a density of 1590 kg/m³ and the silicone a density of 975,6 kg/m³ (Table 1). The density contrast between these materials differs from that between an overburden layer of limestones, sandstones and turbidites ($\rho = $ ~2500 kg/m³) and a basal layer of rocksalt ($\rho = $ ~2160 kg/m³) in nature, which is ~340 kg/m³. Therefore, the silicone has been mixed with dense iron powder to establish a nearly identical density contrast between the experimental materials of 349 kg/m³ (Table 1). Sand acts as frictional plastic material that fails according to the Mohr-Coulomb failure criterion and is generally considered as a suitable material to model brittle deformation of the continental crust (Mandl et al., 1977; Lohrmann et al., 2003). The

quartz sand that was used during modelling is quite angular and has an internal friction coefficient of ~0.88–0.89 and the cohesion is modelled as zero, which is typical for dry sand in analogue models (Schellart, 2000; Graveleau et al., 2012). Due to the model thickness of the experiments the influence of compaction can be neglected as well (Schellart, 2000). Within the constant-thickness PDMS-iron layer, the maximum shear strain rate was 0.0003 s⁻¹, giving a viscosity of 71 × 10³ Pa s as measured by an Anton Paar MRC 702 Twin Drive Rheometer at 20 °C (Fig. 4). Within the wedge-shaped viscous body, the maximum shear strain rate decreased from west (0.003 s⁻¹ for ~1 mm thick PDMS-iron mixture) to east (0.0003 s⁻¹ for 10 mm thick PDMS-iron mixture), and within this strain rate range the viscous mixture behaved in an approximately Newtonian fashion with a viscosity in the range 62–71 × 10³ Pa s (Fig. 4). The experimental viscosity scales to a viscosity for rocksalt in nature of 6.6–7.6 × 10¹⁸ Pa s by using the scaling equation 12 from Schellart and Strak (2016):

$$\frac{\eta^m}{\eta^p} = \frac{\Delta\rho^m \, l^m \, t^m}{\Delta\rho^p \, l^p \, t^p} \tag{1}$$

Here, η is the dynamic shear viscosity, $\Delta\rho$ is the density contrast, l is the length scale and t is time, while superscripts m and p indicate model and natural prototype, respectively. The effective viscosity calculated in this study lies in the estimated range for natural rocksalt (10^{17}–10^{20} Pa s) calculated by van Keken et al. (1993).

4. Results

4.1. Experiment without a weak basal silicone layer

In experiment 4, which was conducted without a basal viscous sheet, a total of five major thrusts formed sequentially striking ~ perpendicular to the shortening direction during 24 cm of shortening (Fig. 5). Fault spacing of newly formed thrusts with respect to previously formed thrusts ranged between ~5 cm and ~15 cm. Except for the third thrust, all thrusts continued along the entire width (parallel to the strike of the backstop) of the experimental set-up. During shortening seven back thrusts developed on top of previously formed thrusts and grew laterally over time. As shortening continued, the wedge thickened and progressively widened through imbrication and grew outward as new thrusts formed. At the end of the experiment the propagation front was 54 cm away from the initial backstop location, which corresponds to 27 km in nature.

In the cross-section that was cut through the centre of experiment 4, five thrusts and seven back thrusts are distinguished by tracing the black marker layers (Fig. 6). The three thrusts closest to the backstop show close proximity to each other (horizontal separation of 1.5 and 2 cm)
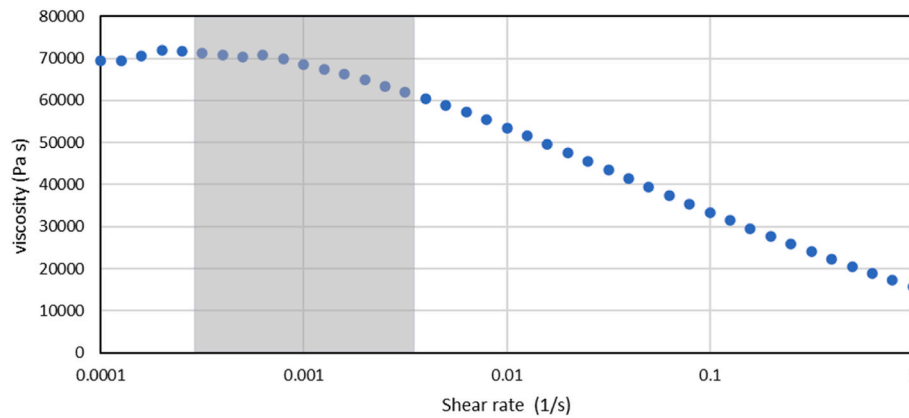
Fig. 4. Diagram showing the dependence of the effective dynamic shear viscosity of the silicone-iron powder mix on the shear rate (x-axis) at room temperature (20 °C). The experimental shear strain rates are shown with the grey-shaded area and show that in this strain rate range the silicone-iron powder layer behaves in an approximately Newtonian manner. The data were obtained by using an Anton Paar MCR 702 Twin Drive Rheometer.

with an average dip angle of 46–50°. Whereas the fourth and fifth thrusts show a larger fault separation (5 and 8 cm) and are characterised by shallower dip angles at the base, progressively shallowing to 15–30° at the surface. All thrusts branch from the basal detachment horizon and the older thrusts are cut by back thrusts. Like the thrusts, the back thrusts also occur in closer proximity to each other near the backstop and are more widely spaced towards the deformation front. Except for b4, all back thrusts have nucleated on a thrust. More so than for the thrusts, the thrust angles within the back thrusts differ in steepness. The two back thrusts closest to the backstop have dip angles of 63–65°, whereas the cluster of four back thrusts in the middle show dip angles between 40 and 50°. The back thrust furthest away from the backstop has an average dip of 51°.

4.2. Experiment including a viscous basal layer (Exp. 8)

The structural evolution of experiment 8 with a weak basal viscous layer set-up, as shown in Fig. 3 (right), is described below. Another experiment with the same model set-up has been conducted (experiment 7) to ensure reproducibility (see Appendix A).

During the first 25% (5 cm) of the total shortening two major thrusts (numbered 1–2), two minor thrusts (not numbered because they do not surface) and two back thrusts (b1-b2) develop (Fig. 7A). The first thrust initiates in the high basal friction (sandy) part of the experiment and reaches the surface at 8 cm distance from the backstop and propagates sub-parallel to the backstop towards the east (towards the sand-viscous domain). Before the second major thrusts nucleates, two small thrusts appear on top of the first thrust sheet. The second major thrust again initiates in the sandy part of the experiment and propagates towards the sand-viscous domain. When reaching the transition zone, the fault trace changes orientation and curves ~80° clockwise and propagates ~6 cm towards the foreland, after which the fault trace changes orientation again and curves ~80° back again to continue in the sand-viscous domain, running sub-parallel to the backstop. In the sand-viscous domain, a back thrust forms simultaneously (b1) in the hanging wall of the new thrust, causing a basin to form between the first and second thrusts.

At 25–50% (5–10 cm) of shortening several additional thrusts and several additional back thrusts form along with progressive steepening of the earlier formed faults, while the wedge progressively grows and increases in height (Fig. 7B). The model height in the sand-only domain increases more rapidly and the taper angle is higher than in the sand-viscous domain due to a higher amount of stacking of the thrust sheets in the former domain. In the high basal friction zone, the fault density is higher than in the low basal friction zone. Thrust number three nucleates simultaneously within the sand-viscous domain and sand-only

domain and merges with the second thrust in the transition zone. With continued progressive backstop motion, a new thrust (4) and back thrust (b3) form simultaneously in the sand-viscous domain (Fig. 7B). An unwanted boundary effect (shear drag) is visible at the eastern sidewall of the experiment in the sand-viscous domain, which gives the faults a curved geometry within 10 cm from the side wall (Fig. 7B–D). In the transition zone the new fault traces also curve towards the backstop in a similar way as thrust number two. Both the thrust and back thrust do not continue further but terminate at high angle against earlier formed thrusts three and two, respectively.

At 50–75% (10–15 cm) of shortening, earlier formed faults continue to steepen, several small thrusts and back thrusts form and the existing back thrusts grow laterally (Fig. 7C). In the sand-viscous domain a large thrust forms in close proximity to thrust number 4 and merges with this thrust in the transition zone. The transition zone develops new and relatively small fault structures that do not extend towards the sand-only or sand-viscous domains.

At 75–100% (15–20 cm) of total shortening a last thrust (6) and back thrust (b8) develop simultaneously in the sand-viscous domain and propagate towards the sand domain while developing an oblique structure in the transition zone that makes an angle of ~55° with the backstop (Fig. 7D). Furthermore, during this stage bulk shortening of the wedge induces imbrication of previous existing structures, increases the height of the model, causes existing faults to steepen and leads to further development of both thrusts and back thrusts. In the transition zone, multiple smaller thrusts and back thrusts form to account for the difference in foreland displacement between the sand-only and sand-viscous domains. At the lateral sides of the experimental domain, the fault traces curve towards the edge of the side-walls, but the curves at the sand-viscous side are wider, forming curved fault traces near the side wall, especially in the youngest two thrusts. At the end of the experiment the deformation front was 68 cm away from the initial backstop location.

In cross-section *exp8-1* in the sand-only domain four thrusts and five back thrusts can be distinguished by tracing the (originally horizontal) black marker layers (Fig. 9A). The two oldest thrusts are cut and off-set by back thrusts multiple times. The thrusts range in dip angle between 40 and 50° with a decrease in dip angle towards the foreland. All thrusts are steepest at the base and decrease in dip angle towards the surface, reaching dip angles as low as ~15–25° near the surface for thrusts 3 and 6. The back thrusts increase in steepness with age. The oldest back thrust dips at 72° and the youngest at 45°. All thrusts and three out of five back thrusts nucleate at the base. The remaining two back thrusts nucleate at previously formed thrusts.

In cross-section *exp8-2* of the transition zone perpendicular to the shortening direction eight thrusts and six back thrusts can be
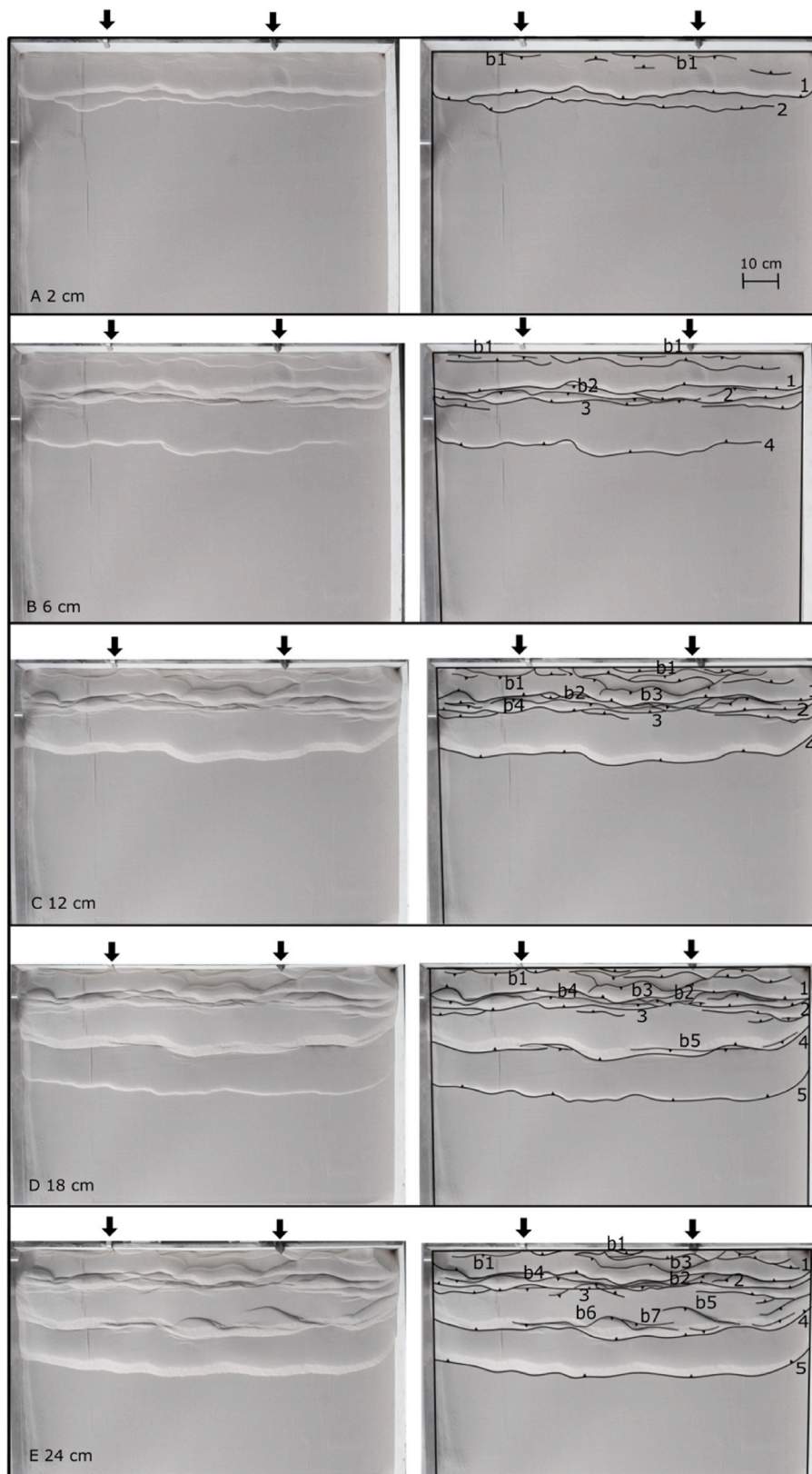
Fig. 5. Top view photographs of experiment 4 with a 4 cm sand cover without (left) and with (right) line drawing interpretations of fault patterns. The backstop is represented by the black arrows and located at the top of each image, moving towards the bottom of each image. The major thrusts that are described in the text are numbered 1–5. Back thrusts are numbered b1-b7. Total shortening during the experiment was 24 cm. A) 2 cm of shortening. B) 6 cm of shortening. C) 12 cm of shortening. D) 18 cm of shortening. E) 24 cm of shortening.

Fig. 6. Side view photograph of cross-section of experiment 4 without (A) and with (B) line-drawing interpretation. Cross-section runs through the centre of experiment 4 (normal to the strike of the backstop). Cross-section was cut after completion of the model run. Ruler (with numbers in mm) shows scale. In the interpretation, dashed lines indicate thrusts, while dotted lines indicate back thrusts. The numbers correspond with the numbers in Fig. 5 to indicate specific faults. Note that the green material at the top surface of the model was added after completion of the experiment. (For interpretation of the references to colour in this figure legend, the reader is referred to the Web version of this article.)

distinguished due to disturbances in the black marker layers (Fig. 9B). All thrusts that nucleated in the viscous layer cause deformation of the viscous layer and at some localities small volumes of it detach from the basal viscous layer. Both the youngest thrust and back thrust show a 30° dip angle, all older thrusts and back thrusts have dip angles between 30° and 40°. The thrust closest to the backstop is cut and offset by back thrusts. The second oldest thrust is a blind fault that does not reach the surface. None of the back thrusts are offset by a thrust.

The cross-section of the low basal friction, sand-viscous domain *exp8-3* is similar to that of the transition zone *exp8-2* (Fig. 9). However, in the thicker part of the viscous layer more displacement and detachment occurs than in the thinner equivalent. All thrusts nucleate at the viscous layer and the piggy-back basins are more developed than in the sand-only domain and transition zone. Both thrusts and back thrusts have angles between 30° and 40°. In the sand-viscous domain and to a lesser extent in the transition zone the pop-down structures are tilted up to ~10° towards the foreland.

Oblique cross-sections of experiment 8 are presented to better understand and analyse the oblique thrust structures visible in the experiment (Figs. 8 and 10). Cross-section *Exp8-4* is the most frontal oblique section and shows a simple pop-up structure with conjugate faults with 35–40° angles that occurred at the surface of the deformation front near the edge of the viscous layer. Both the thrust and back thrust developed within the weak detachment layer (Fig. 10A). Close to the corner (dashed line) another thrust is visible. The next cross-section (*exp8-5*) shows, in addition to a pop-up structure that also has 35–40° fault angles, two separate thrusts dipping at 25–30°. The back thrust of the pop-up structure cuts off one of these previously formed thrusts (Fig. 10B). In this cross-section no structures propagate further than the viscous layer. Moving towards the high friction zone cross-section *exp8-6* only shows three thrusts that are not accompanied by any back thrusts. They all occur within the very thin viscous layer on the transition zone and demonstrate fault angles between 30 and 35°. The middle fault displaces some of the viscous mixture along the fault plane (Fig. 10C). The final oblique cross-section, *exp8-7*, contains three thrusts and one back thrust (Fig. 10D). All faults have approximately the same angle (40°) and the back thrust and oldest two thrusts form a pop-up structure that displaces some of the viscous layer forming a small dome.

## 5. Discussion

5.1. Comparison between experiments

In both experiments thrusts and back thrusts developed perpendicular to the shortening direction. However, in experiment 4 (sand only) the fault traces form relatively continuous straight lines running parallel to sub-parallel to the backstop, whereas the faults in experiment 8 (sand + PDMS-mixture) show significant curvature of the fault traces in the western part of the transition zone, striking at high angle (up to 90°) to the strike of the backstop. In several cases faults in experiment 8 terminate near the transition zone or merge with other faults. Experiment 4 and the western (sand only) part of experiment 8 are very similar in the amount of thrusts, their placement within the model and fault angle. However, in contrast to experiment 4, experiment 8 shows lateral differences in topography, deformation front propagation, lateral change in deformation style, side-wall drag effect and back thrust development. Also, the extent of side-wall drag effects, which occur because of friction between the wedge material and the lateral side-walls (e.g., Schreurs et al., 2006), is smaller in experiment 4 than along the eastern side wall in experiment 8 due to the presence of the viscously deforming basal layer. Total shortening for experiment 4 and supplementary experiment 7 are both 24 cm whereas total shortening for experiment 8 is 20 cm. This difference is simply due to technical issues with the piston after completing experiment 7, which, after repairs, allowed for a maximum shortening of 20 cm. Nonetheless, experiment 8 experienced enough shortening to develop and study the oblique faulting in the transition zone, and also allowed us to study possible rotation due to the addition of rotation markers.

5.2. Model differences caused by the introduction of the basal viscous layer

Differences in structures, topography and kinematics between experiments 4 and 8 are caused by the viscous layer that was introduced in experiment 8. The most striking observation is the differential propagation of the deformation front between the high basal friction zone in the west and low basal friction zone in the east of experiment 8. A displacement discontinuity between the zones causes oblique fault structures to develop since the deformation front of the low basal friction zone propagates faster than in the high basal friction zone (Figs. 7 and 11), in agreement with earlier modelling studies (e.g., Calassou et al., 1993; Cotton and Koyi, 2000; Vidal-Royo et al., 2009; Bose et al., 2015). Within the high basal friction zone thrusts at the deformation front nucleate with a dip angle of about 45° and in the low friction zone with a slightly lesser angle (40°) as is expected according to the Mohr-Coulomb theory (Labuz and Zang, 2012). After deformation propagation, earlier formed faults in the high friction zone rotated towards steeper angles, and in the low friction zone new thrust faults form
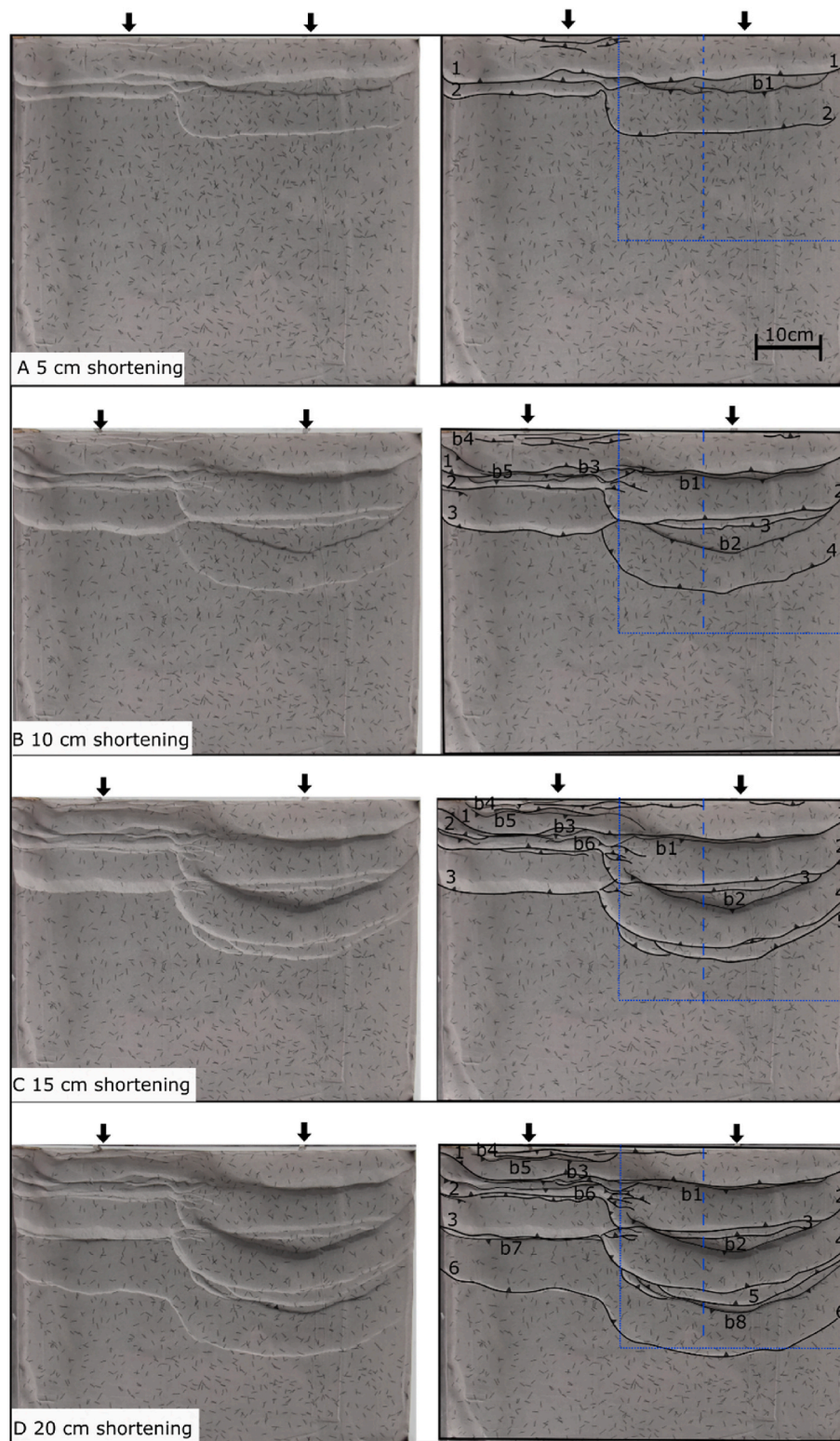
Fig. 7. Top view photographs (left and right) and line drawings of fault patterns (right) of experiment 8 with a 4 cm sand cover on the left side of the experiment and a 1 cm viscous sheet topped with 3 cm sand on the right side of the experiment (right blue dotted line to dashed blue line). In the middle of the experiment the viscous sheet gradually thins westward and sand thickness increases accordingly (dashed blue line to left blue dotted line). Shortening is imposed from the north as visualized by the black arrows representing the backstop. The total amount of shortening of the experiment is 20 cm. The major thrusts that are described in the text are numbered 1–6. Back thrusts are numbered b1-b8. A) 5 cm of shortening. B) 10 cm of shortening. C) 15 cm of shortening. D) 20 cm of shortening.
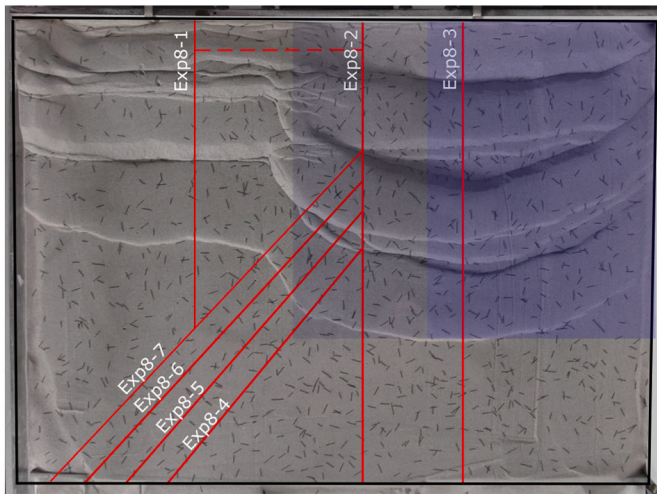
Fig. 8. Top view photograph of experiment 8 at the end of the experimental run (100% deformation) showing the location of the cross-sections (red lines), topographic comparison with the Ainsa oblique zone (red dashed line) and the location of the basal viscous sheet (blue rectangle). The light blue/grey zone in the centre visualizes the wedge-shaped part of the basal viscous sheet that thins towards the left (westwards). Dimensions of the viscous sheet and sand cover are shown in Fig. 3. The cross-sections are displayed in Figs. 9 and 10. (For interpretation of the references to colour in this figure legend, the reader is referred to the Web version of this article.)

at the deformation front, which is consistent with earlier experimental work (Fig. 9; Mulugeta, 1988; Calassou et al., 1993; Cotton and Koyi, 2000; Bose et al., 2009). The weight of the overburden on the viscous layer caused displacement of the viscous material into the thrust planes and along back thrusts, which leads to the development of small salt domes at the bottom of several thrusts in the experiment, as also observed in earlier work (Cotton and Koyi, 2000; Vidal-Royo et al., 2009).

In the high friction zones of the experiments shortening leads to compaction, rotation and the formation of a relatively rigid imbricate moving block. The low friction zone first accommodates shortening through thrust propagation while also forming piggyback basins before slight compaction and rotation. This difference in deformation style between the high and low basal friction zones causes a discontinuity in topographic height due to the difference in critical taper angle between the domains (Davis et al., 1983; Mulugeta, 1988; Dahlen, 1990; Calassou et al., 1993; Cotton and Koyi, 2000; Vidal-Royo et al., 2009; Graveleau et al., 2012). The transition between high and low friction is characterised by a complex area where structures of both friction zones interact to form a mixed geometry consisting of elements from both friction zones (Figs. 9 and 10, Calassou et al., 1993; Schreurs et al., 2001; Santolaria et al., 2022). The most obvious features of the transition zone are the oblique thrust fault structures which connect the thrusts that propagated with different velocity. Fig. 11 shows this difference in thrust propagation by visualizing the horizontal displacement field of passive black markers. It is evident that horizontal displacement of material in the low friction zone occurs further away from the backstop than in the high friction zone, inducing a large-scale dextral shear in a north-south direction that is accommodated by the transition zone. The horizontal displacement only occurs perpendicular to the backstop, even in the oblique fault zones. This means there has not been a significant change in stress field orientation and that the oblique thrust faults experience dextral shearing in the transition zone (Graveleau et al., 2012), causing the local rotations that are observed in Fig. 12. In the transition zone and the imbricated part of the high friction zone mostly clockwise rotation of the passive black elongated markers occurs as a result of this dextral shearing (Fig. 12). The highest amounts of clockwise rotation are located close to the oblique thrust fault structures, because the dextral shearing

is most pronounced at these faults. Thus, clockwise rotations within the sand layer occur as a result of local dextral shear instead of regional block rotations, because horizontal displacement remains perpendicular to the shortening direction. Rotation in the transition zone is in accordance with the oblique fault and fold structures presented in the oblique cross-sections and the result of a dextral shearing component due to differential deformation propagation over contrasting basal friction domains (Fig. 10; Reiter et al., 2011; Graveleau et al., 2012; Tavani et al., 2015). Three cases of counter-clockwise rotation have been recorded, which is opposite to what is predicted by the dextral shear experienced at the transition zone. Two of the three counter-clockwise markers are located relatively close to the backstop and their counter-clockwise rotation might be a result of bulk N–S shortening of the ambient granular material. The last rotation marker is located on the axis of a pop-up anticline and might have shifted due to the convex surface. On top of the oblique faults transverse anticlines border basins that developed in the transition zone on the high friction side. On the low friction side, the piggyback basins are bordered by connecting thrust faults or lower transverse anticlines, which is due to the differences in taper steepness between both zones (Davis et al., 1983).

5.3. Comparison between experiment 8 and the Ainsa oblique zone in the Pyrenees

In experiment 8, thrust faults in both friction zones are connected by oblique thrust faults in the transition zone. This is similar to the natural counterpart within the southern Central Pyrenees (Vergés et al., 2002; Vidal-Royo et al., 2009; Muñoz et al., 2013). Fig. 13 shows differential propagation of the deformation structures in the Bóixols, Montsec and Serres marginals thrusts connected by oblique thrust faults in similar fashion to the structures in experiment 8. In the Pyrenees oblique faulting occurs in the Ainsa oblique zone where the Triassic evaporites reduce in thickness from east to west until they are absent. Oblique faulting in the experiments occurs at the transition zone between PDMS-iron powder mixture and sand at the base (Fig. 13). Therefore, the experimental results confirm that a lateral, orogen-parallel, change in basal friction due to the lateral (westward) thinning and disappearance of a weak basal detachment layer, namely the Triassic salt layer, influences the propagation distance of the deformation front and causes oblique dextral thrust faulting and clockwise rotation in the transition zone. Similar findings are reported in other studies simulating lateral, orogen-parallel, differential basal friction (e.g. Calassou et al., 1993; Cotton and Koyi, 2000; Vidal-Royo et al., 2009). The experimental oblique thrust faults that form above the transition zone generally strike NW-SE to N–S with angles between 50° and 90° with respect to the main strike of the fold-and-thrust belt (backstop) (Fig. 13). The oblique structures in the Pyrenees show similar angles with respect to the main strike of the orogen (~60°–90°). The cross-sections in Fig. 9 show that there is a lateral increase in topography towards the high friction zone, showing the increasing influence of the high friction zone deformation style due to a progressively thinning weak basal layer. This is also observed in the Ainsa oblique zone where the topography in the oblique zone gradually rises. The average slope perpendicular to the oblique structures of the cross-sections in Fig. 10B–D is 7.8°, whereas the average oblique orogenic slope of the Ainsa oblique zone is 5.5°. The locations of the cross-sections of the Ainsa oblique zone and experiment 8 can be found in Figs. 2 and 8 respectively. The difference between the slope averages of the experiment and the Ainsa oblique zone is likely, at least partly, because the present-day topographic slope of the Ainsa oblique zone is probably less than the topographic slope in the geological past during its formation due to post-deformation erosion in the Ainsa oblique zone.

Comparison of vertical axis rotations as observed in experiment 8 and as derived from paleomagnetic studies in the Ainsa oblique zone as reported in Muñoz et al. (2013) shows both similarities and differences. In both studies rotation markers indicate clockwise rotation, but
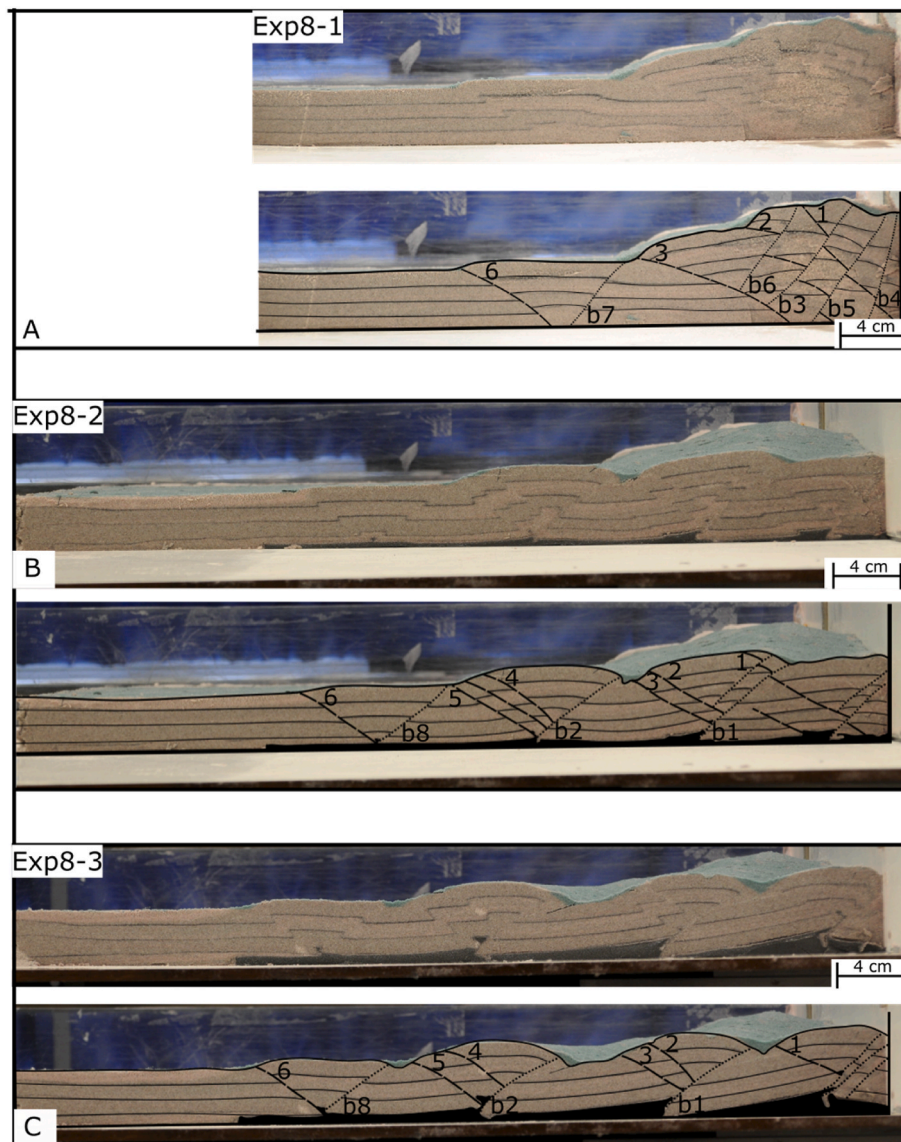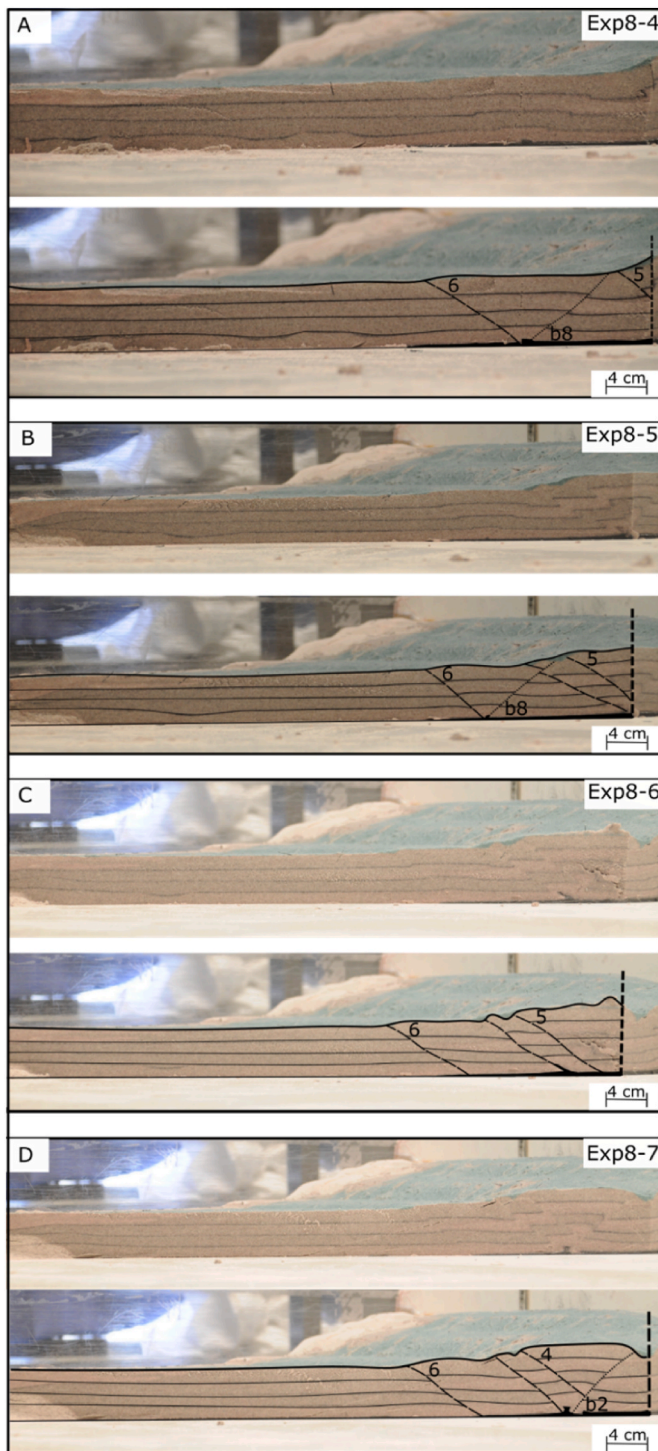
Fig. 9. Side view photographs of cross-sections of experiment 8 either without (top panel) or with (bottom panel) line drawing interpretation of fault pattern, taken parallel to the shortening direction. Cross-section Exp8-1 is located in the sand-only domain, cross-section Exp8-2 is located in the transition zone (sand-PDMS mix layering with the wedge-shaped basal viscous layer), and cross-section Exp8-3 is located in the sand-PDMS mix domain with the constant thickness basal viscous layer. Exact locations of the cross-sections are shown in Fig. 8. In the interpretations, dashed lines indicate thrusts, while dotted lines indicate back thrusts. The numbers correspond with the numbers in Fig. 8 to indicate specific faults. Only the major surfacing faults are numbered, therefore not all fault structures in the cross-sections are numbered. The backstop is located on the right-hand side of the images.

rotation angles measured in the model are smaller (up to 40°) than in the Pyrenees (up to 70°). The difference in rotation magnitude likely results from the difference in rheology of the cover sediments that lie on top of the weak viscous detachment layer in model and nature. The overburden in the experimental model consists only of quartz sand, which has a frictional-plastic rheology, mimicking the average rheology of brittle sedimentary rocks. The rocks in the southern Central Pyrenees are strongly layered and include brittle and ductile rheologies. Quartz sand in the analogue models cannot completely account for the complex brittle-ductile deformation behaviour of the rheologically layered lithologies present in the Pyrenees. Also, the backstop of the experiment is completely straight and vertical, which does not 100% accurately represent the Pyrenean axial zone that acts as backstop (Fig. 13). The combined effect of these, and possibly other, simplifications could be the cause for the smaller experimental rotations in the transition zone compared to those in nature (Calassou et al., 1993; Teixell and Koyi, 2003; Graveleau et al., 2012). Nonetheless, the current analogue

modelling study is consistent with the outcomes of the study of Muñoz et al. (2013), who concluded that rotation in the oblique zone is very likely caused by a discontinuity in basal friction.

Not only the fault orientations produced in the analogue models match those of the Pyrenees, but the anticlinal and synclinal structures as well. In the Pyrenees most anti- and synforms developed parallel to the axis of the orogen (~WNW-ESE), which is to be expected in a convergent fold-and-thrust belt setting. However, in the transition zone where thrust faults show obliquity, the anti- and synforms also demonstrate NNW-SSE to NNE-SSW orientations (Fig. 13). This corresponds with the structures observed in the experimental models, where in the transition zones the anti- and synforms also change orientation since they formed as box folds on top of the thrust ramps (Fig. 7). These antiforms border basins within the model just like the Boltaña and Mediano anticlines border the Ainsa basin in the Pyrenees (Fig. 13). The model depicts that antiformal stacking on thrust ramps with a viscous substrate is favoured over imbrication. The Boltaña and Mediano

Fig. 10. Side view photographs of cross-sections of experiment 8 either without (top panel) or with (bottom panel) line drawing interpretation of fault pattern, oriented obliquely to the shortening direction and located in the transition zone of the wedge-shaped basal viscous layer. The exact location of each cross section is shown with the corresponding lines in Fig. 8. In the interpretation, dashed lines indicate thrusts, while dotted lines indicate back thrusts. The numbers correspond with the numbers in Fig. 7 to indicate specific faults. Only the major surfacing faults are numbered, therefore not all fault structures in the cross-sections are numbered. The backstop is located to the right of each image out of view. The thick black vertical dashed line represents the intersection line with the cross-section oriented parallel to the shortening direction.

anticlines are natural evidence of the same behaviour of the Keuper layer within the Pyrenees on a regional scale (Muñoz et al., 2013). A noticeable difference between model and nature is the number of folds. In the Pyrenees folds dominate and are less frequently accompanied by faults that reach the surface than in our experiments. This structural difference between nature and model is likely caused by the rheological difference between the sedimentary rocks in nature, which show both brittle and ductile behaviour, and the sand layer in the model, which only shows brittle behaviour (Teixell and Koyi, 2003).

Furthermore, taper angles measured in the experiments show a decrease in steepness from the high friction zone (12°) through the transition zone (8°) to the low friction zone (4.5°). The taper angle of the low friction zone is representative for the taper angle of 5° in the southern Pyrenees whereas the taper angle of the high friction zone is representable for general fold-and-thrust belts. The secondary slope caused by the topographic differences between the high and low friction zones (measured along the orogenic axis/along the backstop) were 10° and 12° in nature and experiment, respectively (Figs. 2 and 8). The minor differences between the slope and taper angles of the experiments and nature are within the error margin of the measurements, which indicates that the experimental set-up was able to reproduce a fold-and-thrust belt that behaves according to the critical taper theory (Davis and Engelder, 1985; Meigs and Burbank, 1997).

When comparing the cross-sections obtained during the experiments with the cross-sections of the Ainsa oblique zone by Muñoz et al. (2013) similarities are evident. Both the experimental and natural geometry are dominated by propagating thrusts of similar angles with displaced ductile material in the centre of folds along the thrusts (Fig. 14A). Anticlinal forms on top of thrust are often broken and asymmetrical. The synclines in between are open and contain low flank angles. If a viscous substrate is present, it infiltrates the thrusts and back thrusts bordering the synclinal structure (Fig. 14B).

5.4. Comparison of current experiments with earlier studies

In the past multiple studies involving lateral variation in basal friction and transfer zones have been conducted. Mulugeta (1988) already noted that parameters such as rheology of individual layers, the amount of basal friction, sedimentary load and gravity influence the propagation of thrust wedges and should be considered while trying to produce an analogue model of a natural counterpart. This is evident in the current experiments since variability in propagation distance between zones with different basal friction is the key parameter in explaining the obliqueness and curvature of folds and thrusts in the Southern Central Pyrenees. This study agrees with the studies of Calassou et al. (1993), Schreurs et al. (2001), Bahroudi and Koyi (2003), Luján et al. (2003) and Milazzo et al. (2021), which focussed on transfer zones. All with slightly different set-ups, they concluded that oblique ramps occur at experimental discontinuities in basal friction or passive offset of the backstop. This is caused by the velocity discontinuity between friction zones, which invoked differentiation of frontal propagation and accompanying rotation patterns. The propagation differentiation is the main cause for oblique fold and fault structures and the occurrence of a transition zone that displayed a mixed structural style. Even though slightly different geometries between experiments are present due to the placing and thickness differences of the viscous sheets between the studies, they find that forward propagation of the deformation front over a weak basal layer is more significant than over a stronger basal layer and that the geometry and topographic expression of the transition zone is based on the subsurface rheological changes, which is consistent with the current study.

Lickorish et al. (2002), Farzipour-Saein and Koyi (2014) and Santolaria et al. (2022) focussed on the effects of lateral variation in thickness of a weak decollement by using normal gravity sandbox models or centrifuge models. Lickorish et al. (2002) found that the evolution of the Jura arc was heavily influenced by the presence of
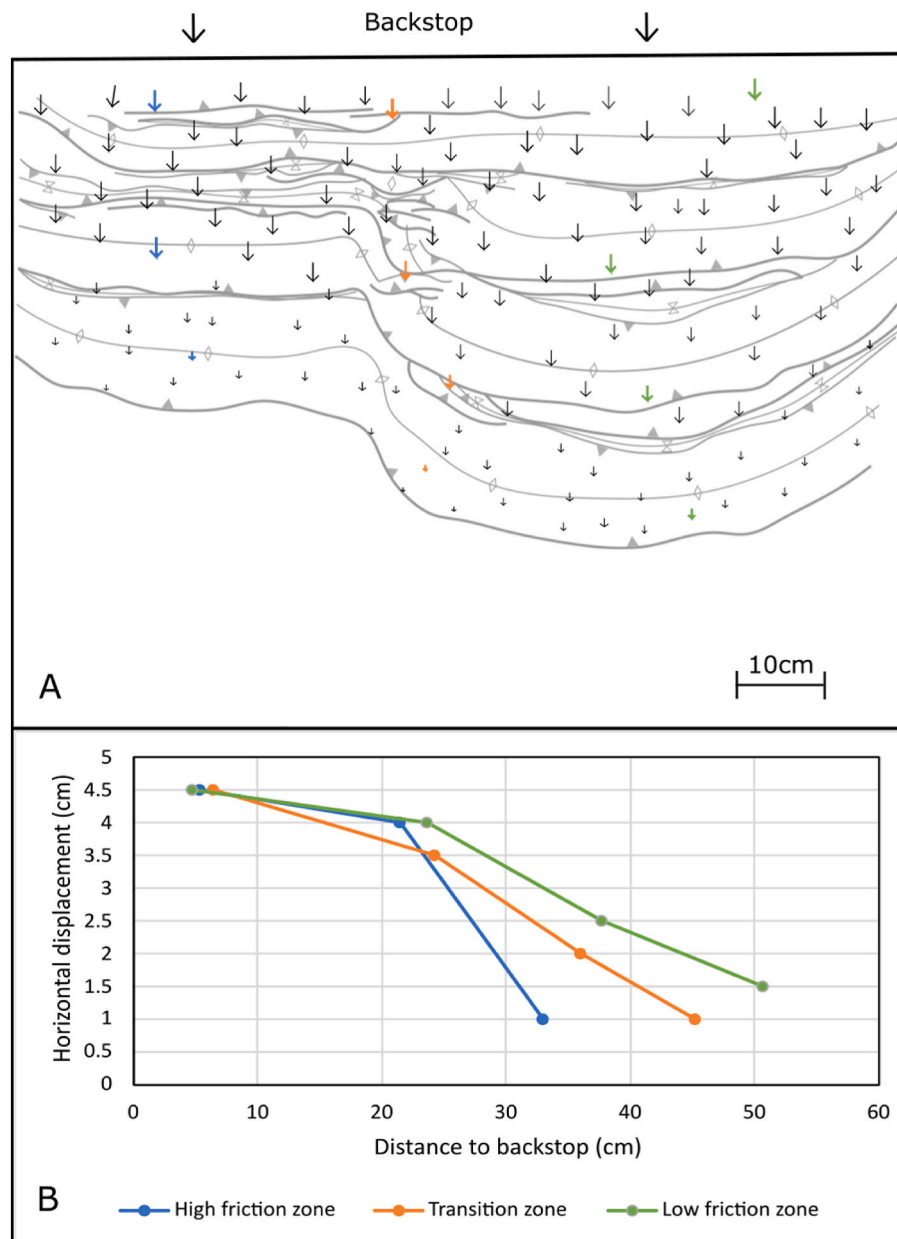
Fig. 11. A) Schematic overview of the horizontal displacement field between 15 cm (75%) and 20 cm (100%) shortening in experiment 8. The arrows are based on the amount of displacement of the passive black markers on top of the experiment measured by tracing their locations between 75% and 100% shortening. B) Line diagram that visualizes the amount of horizontal displacement per domain for the high basal friction zone, transition zone and low basal friction zone as a function of distance from the moving backstop. The amount of horizontal displacement is derived from the respective coloured arrows per domain in the top overview.

Triassic evaporites, similarly to what we propose for the Ainsa oblique zone. Furthermore, Lickorish et al. (2002), Farzipour-Saein and Koyi (2014) and Santolaria et al. (2022) found that a change in lateral thickness of the weak decollement affects deformation style, but their brittle-viscous modelling set-ups did not allow for a strongly defined transition zone with high oblique angles to develop, as needed for the Ainsa oblique zone. The experimental set-up for decreasing thickness of the viscous layer used by Lickorish et al. (2002) involved a step-wise thickness decrease reducing the viscous layer thickness within individual sheets of constant thickness with approximately 50% each step. The sheets were of equal lateral size aside from the middle sheet. This set-up was sufficient for explaining the influence of Triassic evaporites on the evolution of the Jura arc, but not sufficient to form the high angle oblique transition zone required to explain the Ainsa oblique zone.

The study of Cotton and Koyi (2000) investigated the behaviour of salt in thrusts and detachments. Their findings included the possibility of salt diapirs when anticlines containing salt in the cores are eroded. Salt domes occur southwest of the study area in the Pyrenees as well (Vidal-Royo et al., 2009). However, within the study area salt domes or diapirs are not present, likely because the Triassic salt layer is quite thin in the Ainsa basin and the anticlines have not yet eroded far enough to exhume the salt cores. The study of Cotton and Koyi (2000) also shows that pressure of overburden material causes viscous matter to relocate to positions in areas of lower pressure. As described in the results section on the cross-sections, this process is slightly visible in this study as well but to a lesser extent than in Cotton and Koyi (2000) since our viscous layer is thinner compared to the overburden. Vidal-Royo et al. (2009) focused on the Central External Sierras, a part of the Pyrenees where salt domes do occur and investigated differences in basal friction. Even though a different modelling set-up was applied due to another
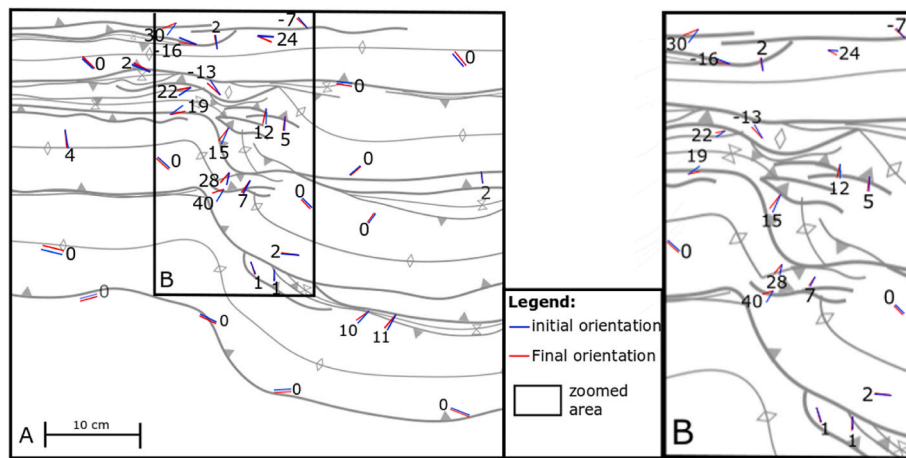
Fig. 12. A) Top view of the central part of experiment 8 showing the total rotation of passive markers (small black elongated cylinders in Figs. 7 and 8) located on top of the experiment. Also shown are the structures at 100% shortening (in grey). B) Zoom-in of the indicated transition zone in panel A. Numbers indicate amount of rotation in degrees, with positive numbers indicating clockwise rotation and negative numbers indicating anticlockwise rotation.
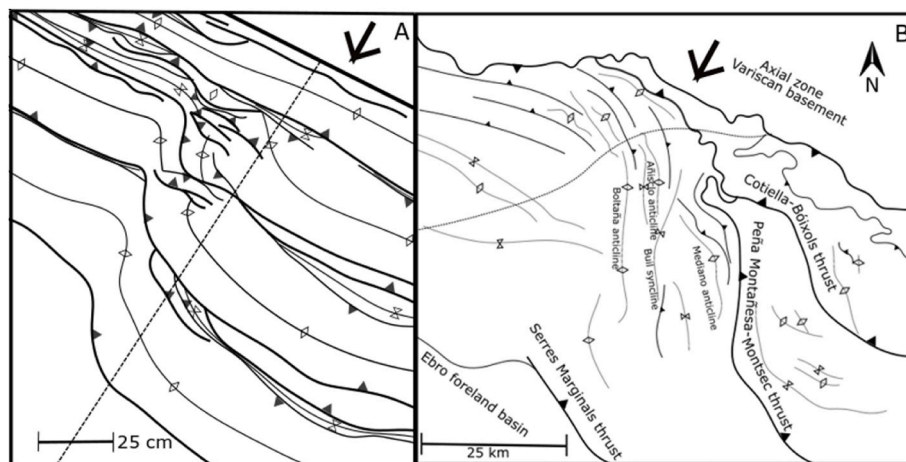

Fig. 13. A. Zoom-in of the top view of the final shortening stage of experiment 8. B. Simplified structural overview of the Ainsa oblique zone modified after Muñoz et al. (2013). The big arrows on top indicate the shortening direction, the dashed lines indicate the end of the viscous layer. Note that the experimental top view has been rotated 33° clockwise such that the orientation of the backstop is parallel to the orogenic axis of the Pyrenees, which strikes WNW-ESE.

geometry of the unevenly distributed Keuper layer at the base, similarities between our study and Vidal-Royo et al. (2009) occur. Both studies agree that curvatures in fold and thrust structures in the Pyrenees developed due to a change in basal friction that led to a velocity discontinuity in the deformation front.

Bahroudi and Koyi (2003), Li and Mitra (2017), Vendeville et al. (2017) and Borderie et al. (2018) mainly focussed on the geometry of transition zones between frictional and viscous basal detachment. They found that the geometry of the deformation front is strongly controlled by the geometry of the detachment boundary (i.e., its orientation with respect to the backstop). Oblique transitions in basal friction account for an oblique deformation front and deformation propagation rate is affected by the thickness of the viscous layer, which also influences the taper angle in the topography. The similarities between Bahroudi and Koyi (2003), and Li and Mitra (2017) and the current study implies that the cover-PDMS-iron mixture ratio of the experiments and geometry of the basal friction boundary most accurately represents the Pyrenees and strengthens our finding that the regional structural style is mainly influenced by the gradual transition between a strong and weak basal detachment zone. The complementary studies of Vendeville et al. (2017) and Borderie et al. (2018) added that the width of viscous zones is important for the deformation geometry and that three structural styles

can be observed in areas affected by a lateral change in friction during shortening. The sloping PDMS-iron mixture ramp introduced in the current study might have acted as a natural buffer between the friction zones and allowed the low friction zone to propagate free of the effects of drag caused by the adjacent high friction zone. Vendeville et al. (2017) stressed that the low critical surface slope angle induced by viscous layers caused the deformation zone to rapidly propagate due to low viscosity of the layer, in contrast to a higher critical surface slope angle in stronger domains. This study agrees with Vendeville et al. (2017) since taper angles in the high basal friction zone are higher (12°) than in the transition zone (8°) and low basal friction zone (4.5°).

Jiménez-Bonilla et al. (2020) used a slightly different approach than the previously mentioned studies. They used sand only and sand-silicone models without a lateral friction variation and a flexible backstop to model the Gibraltar arc. The backstop that they used increased in curvature over the duration of the experiments. The displacement field generated from their model set-up showed a radial pattern with both inwards and outwards directed vectors approximately perpendicular to the thrust faults. This differs greatly from experiment 8 in our study where the displacement field is unidirectional and parallel to the displacement direction of the backstop, approximately perpendicular to the strike of the thrust faults in the low-friction and high-friction
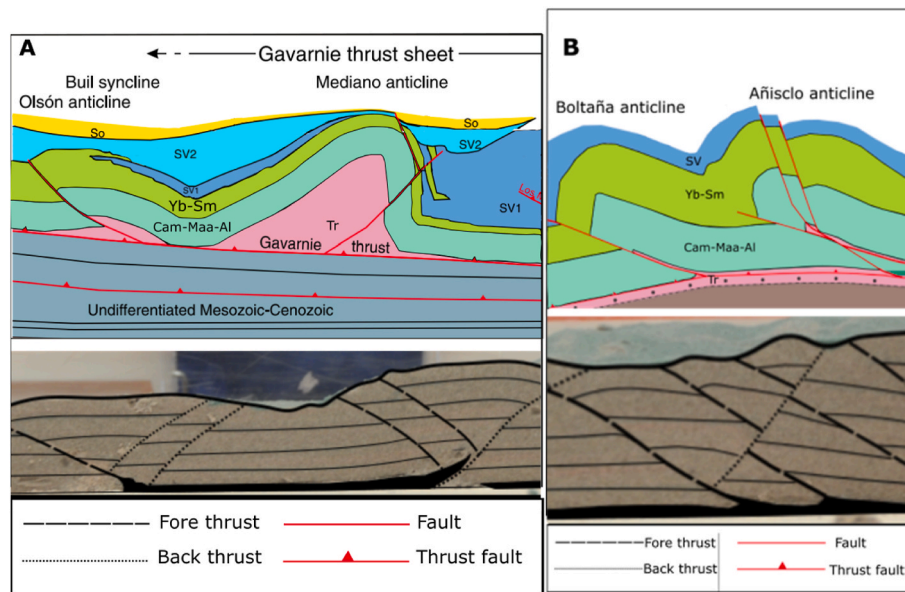
Fig. 14. A) Zoom-in of cross-section, simplified after Muñoz et al. (2013), compared to a zoom-in of cross section exp7-2. Both cross-sections show an open syncline with ductile material displacement into the faults. B) Zoom-in of cross-section, simplified after Muñoz et al. (2013), compared to a zoom-in of cross section exp7-2. Both cross-sections show viscous material in the core of anticlinal stack structures along thrusts. In all images the backstop is located out of view on the right-hand side. For the experiments the backstop is perpendicular to the cross-sections whereas the cross-sections of Muñoz et al. (2013) are taken obliquely (45°) to the shortening direction. Tr: Triassic, Cam: Campanian, Maa: Maastrichtian, Al: Alveolina limestones, Yb: Yeba, Sm: Santa Marina, SV1-SV2: San Vincente Formation.

domains, and with an oblique angle to the strike of the thrust faults in the transition zone.

Llavall and Sainz (2012) conducted the only other study with a sloping viscous ramp. The slope angle and thickness of the silicone layer was altered between experiments, which led them to conclude that fault propagation was faster and further in the thick viscous zone than in the thin viscous zone and when inclination angles where lower and thus silicone layer thickness less variable, back thrusts accommodated more displacement. The current experimental set-up shows several similarities with that of Llavall and Sainz (2012), but with the major differences that we add a zone with a constant thickness of the viscous sheet on one side of the viscous ramp and that our transition zone viscous sheet tapers to 0 mm thickness. This results in highly oblique thrust structures observed in the transition zone in our experiments, striking 50°–90° with the backstop, which are not observed in the experiments of Llavall and Sainz (2012).

One thing that differentiates the current study from all previous studies is the use of a viscous ramp decreasing to 0 mm thickness adjacent to the sand only domain on one side and a constant thickness basal viscous layer on the other side in the experimental set-up. Therefore, the current study most accurately represents a transition zone with a gradual transition between a high and low basal friction zone by thinning of the viscous lithology, as is applicable to the Ainsa oblique zone in the southern Central Pyrenees.

5.5. Model limitations

The Pyrenees are far more complex than the analogue experiments reported in this study. The bottom of the experiments consisted of a rigid, flat, horizontal plate. Thus isostasy, continental subduction, and a dipping basement are not considered. Soto et al. (2006) demonstrated that a basal taper at the backstop also influences thrust propagation. This study excluded a tapered backstop, which is another simplification. Other model simplifications are the constant shortening rate and single-vergent nature of the experiments, while it is known that the Pyrenees are doubly-vergent and have had a variable shortening rate in the past. Shortening velocity can influence deformation propagation (Couzens-Schultz et al., 2003), which has not been considered. The use

of sieved quartz sand simplified the analogue models because such material deforms by faulting instead of folding. Also, the Ainsa oblique zone developed in a syn-sedimentary regime so not all thrusts are currently reaching the surface due to burial. Additionally, exhumation and erosion processes have affected the study area for a long time, which also influenced the area's structural evolution. These processes could not be modelled with the current experimental set-up. The models of this study started with an undeformed sand layer and excluded previously formed extension faults that could be reactivated during a shortening event. Before the Pyrenean orogeny a great extension event took place in the area so pre-existing extension faults were present in the basement prior to Pyrenean orogeny, which might have affected the development of structures that formed during the following period of Pyrenean orogeny. Despite all the above-mentioned experimental simplifications, the experiments have been able to reproduce the plan-view fault and fold structures of the Ainsa oblique zone (Fig. 13) and the clockwise rotations in the transition zone (Fig. 12) are consistent with the rotation direction as implied by paleomagnetic data of the region. As such, the modelling work is consistent with observational studies of the region (e. g., Muñoz et al., 2013), and provides a geodynamic basis for the explanation of the Ainsa oblique zone in the southern Central Pyrenees.

6. Conclusions

In the present experimental study, the oblique structures in the Ainsa oblique zone have been examined by comparing analogue modelling results with the Ainsa oblique zone. The hypothesis that the gradual transition from high to low basal friction in a shortening regime is able to influence the regional structural style and cause oblique fault and fold structures in the Ainsa oblique zone has been confirmed experimentally. Comparison between experiments and nature show that the oblique structures are a product of the sedimentary cover detaching over a high friction zone consisting of brittle rocks and a low friction zone consisting of gradually thinning Triassic evaporites. The deformation front propagates faster over the viscous substrate and favours the formation of thrusts and back thrusts over imbrication and compaction. The high-friction substrate favours imbrication and compaction over fault propagation. Due to the variation in propagation velocity of the deformation

front, induced by the lateral change in basal friction, a transition zone forms, which connects the two domains with different structural styles by oblique faults and folds.

In the transition zone the thrusts of the high and low basal friction zones connect by a change in orientation of the thrusts to strike almost perpendicular to the strike of the backstop. This leads to the ~N–S oriented fault and fold structures in the Pyrenees that break the general WNW-ESE fault and fold orientation in the orogen. Clockwise rotations in the transition zone, observed in both experiment (Fig. 12) and nature, are induced by dextral shear caused by the difference in horizontal deformation propagation between the high and low basal friction zones. Angles of obliquity of the structures in the experiments and in the natural counterpart are similar, which is a good indicator that comparable processes are at play. The oblique orientation of the thrusts is accompanied by the obliquity of anticlines in the transfer zone which form the borders of previously formed basins such as the Ainsa basin in the study area. Both in the experiments and in the Pyrenees a difference in taper angle and topographic height occurs west and east of the transition zone, with in both cases a higher taper angle and topography in the west compared to the east.

Author statement

Iris van der Werf: Writing - Original Draft, Methodology, Validation, Investigation, Visualization, Wouter Schellart: Conceptualization, Methodology, Resources, Writing - Review & Editing, Supervision, Funding acquisition, Vincent Strak: Methodology, Writing - Review & Editing, Supervision, Project administration, Luuk van Agtmaal: Writing - Review & Editing, Ruiz Blankendal: Writing - Review & Editing.

Declaration of competing interest

The authors declare that they have no known competing financial interests or personal relationships that could have appeared to influence the work reported in this paper.
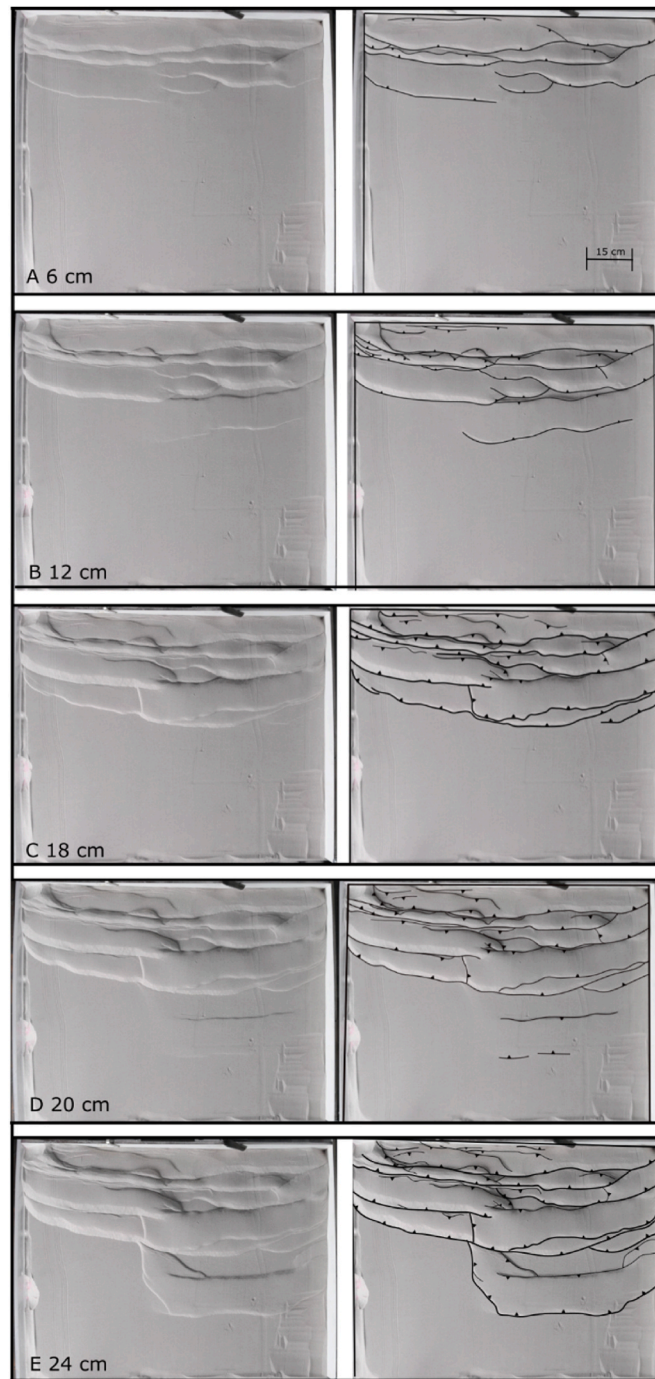
Data availability

Data will be made available on request.

Acknowledgements

Appendix A. Experiment 7

Fig. A1. Top view photographs (left and right) and line drawings of fault patterns (right) of experiment 7 with the same experimental set-up as experiment 8 (4 cm sand cover on the left side, a 1 cm basal viscous sheet topped with 3 cm sand on the right side of the experiment, and a transition zone in the middle with a gradually westward thinning basal viscous sheet). Shortening is initiated from the top with a velocity of 1 cm/h. Total shortening of the experiment is 24 cm. A) 25% of total shortening. B) 50% shortening. C) 75% shortening. E) 100% shortening. Panel D with 20 cm shortening is added to compare experiment 7 with the end stage of experiment 8.

References

Alonso, J., Pulgar, J., García-Ramos, J., Barba, P., Friend, P., Dabrio, C., 1996. W5 tertiary basins and alpine tectonics in the cantabrian mountains (NW Spain). Tertiary Basins Spain: Stratigr. Rec. Crustal Kinemat. 214–227.

Bakke, K., Gjelberg, J., Petersen, S.A., 2008. Compound seismic modelling of the Ainsa II turbidite system, Spain: application to deep-water channel systems offshore Angola. Mar. Petrol. Geol. 25 (10), 1058–1073.

Bahroudi, A., Koyi, H., 2003. Effect of spatial distribution of Hormuz salt on deformation style in the Zagros fold and thrust belt: an analogue modelling approach. J. Geol. Soc. 160 (5), 719–733.

Beaumont, C., Muñoz, J.A., Hamilton, J., Fullsack, P., 2000. Factors controlling the Alpine evolution of the central Pyrenees inferred from a comparison of observations and geodynamical models. J. Geophys. Res. 105 (B4), 8121–8145.

Borderie, S., Graveleau, F., Witt, C., Vendeville, B.C., 2018. Impact of an interbedded viscous décollement on the structural and kinematic coupling in fold-and-thrust belts: insights from analogue modeling. Tectonophysics 722, 118–137.

Bose, S., Mandal, N., Mukhopadhyay, D.K., Mishra, P., 2009. An unstable kinematic state of the Himalayan tectonic wedge: evidence from experimental thrust-spacing patterns. J. Struct. Geol. 31, 83–91. https://doi.org/10.1016/j.jsg.2008.10.002.

Bose, S., Saha, P., Mori, J.J., Rowe, C., Ujiie, K., Chester, F.M., Conin, M., Regalla, C., Kameda, J., Toy, V., Kirkpatrick, J., Remitti, F., Moore, J.C., Wolfson-Schwehr, M., Nakamura, Y., Gupta, A., 2015. Deformation structures in the frontal prism near the Japan Trench: insights from sandbox models. J. Geodyn. 89, 29–38.

Calassou, S., Larroque, C., Malavieille, J., 1993. Transfer zones of deformation in thrust wedges: an experimental study. Tectonophysics 221 (3–4), 325–344.

Chanvry, E., Deschamps, R., Joseph, P., Puigdefàbregas, C., Poyatos-Moré, M., Serra-Kiel, J., et al., 2018. The influence of intrabasinal tectonics in the stratigraphic evolution of piggyback basin fills: towards a model from the Tremp-Graus-Ainsa Basin (South-Pyrenean Zone, Spain). Sediment. Geol. 377, 34–62.

Choukroune, et al., 1988. The ECORS deep reflection seismic survey across the Pyrenees. Nature 331, 508–511.

Cotton, J.T., Koyi, H.A., 2000. Modeling of thrust fronts above ductile and frictional detachments: application to structures in the Salt Range and Potwar Plateau, Pakistan. Geol. Soc. Am. Bull. 112 (3), 351–363.

Couzens-Schultz, B.A., Vendeville, B.C., Wiltschko, D.V., 2003. Duplex style and triangle zone formation: insights from physical modeling. J. Struct. Geol. 25 (10), 1623–1644.

Dahlen, F.A., 1990. Critical taper model of fold-and-thrust belts and accretionary wedges. Annu. Rev. Earth Planet Sci. 18, 55–99.

Davis, D., Suppe, J., Dahlen, F.A., 1983. Mechanics of fold-and-thrust belts and accretionary wedges. J. Geophys. Res. Solid Earth 88 (B2), 1153–1172.

Davis, D.M., Engelder, T., 1985. The role of salt in fold-and-thrust belts. Tectonophysics 119 (1–4), 67–88.

Dreyer, T., Corregidor, J., Arbues, P., Puigdefabregas, C., 1999. Architecture of the tectonically influenced Sobrarbe deltaic complex in the Ainsa Basin, northern Spain. Sediment. Geol. 127 (3–4), 127–169.

Farzipour-Saein, A., Koyi, H., 2014. Effect of lateral thickness variation of an intermediate decollement on the propagation of deformation front in the Lurestan and Izeh zones of the Zagros fold-thrust belt, insights from analogue modeling. J. Struct. Geol. 65, 17–32.

Fitzgerald, P.G., Muñoz, J.A., Coney, P.J., Baldwin, S.L., 1999. Asymmetric exhumation across the Pyrenean orogen: implications for the tectonic evolution of a collisional orogen. Earth Planet Sci. Lett. 173 (3), 157–170.

Graveleau, F., Malavieille, J., Dominguez, S., 2012. Experimental modelling of orogenic wedges: a review. Tectonophysics 538, 1–66.

Hobbs, W.H., 1914. Mechanics of formation of arcuate mountains. J. Geol. 22 (3), 193–208.

Jiménez-Bonilla, A., Crespo-Blanc, A., Balanyá, J.C., Expósito, I., Díaz-Azpiroz, M., 2020. Analog models of fold-and-thrust wedges in progressive arcs: a comparison with the Gibraltar Arc external wedge. Front. Earth Sci. 8, 72.

Koyi, H., 1995. Mode of internal deformation in sand wedges. J. Struct. Geol. 17 (2), 293–300.

Koyi, H.A., Sans, M., Teixell, A., Cotton, J., Zeyen, H., 2004. The significance of penetrative strain in the restoration of shortened layers—insights from sand models and the Spanish Pyrenees. Thrust Tect. Hydrocarbon Syst.: AAPG Memoir 82, 1–16.

Labaume, P., Séguret, M., Seyve, C., 1985. Evolution of a turbiditic foreland basin and analogy with an accretionary prism: example of the Eocene south-Pyrenean basin. Tectonics 4 (7), 661–685.

Labuz, J.F., Zang, A., 2012. Mohr–Coulomb failure criterion. In: The ISRM Suggested Methods for Rock Characterization, pp. 227–231. Testing and Monitoring: 2007-2014.

Li, J., Mitra, S., 2017. Geometry and evolution of fold-thrust structures at the boundaries between frictional and ductile detachments. Mar. Petrol. Geol. 85, 16–34.

Lickorish, W.H., Ford, M., Burgisser, J., Cobbold, P.R., 2002. Arcuate thrust systems in sandbox experiments: a comparison to the external arcs of the Western Alps. Geol. Soc. Am. Bull. 114 (9), 1089–1107.

Llavall, E.I., Sainz, A.M.C., 2012. Influencia de la variación lateral del espesor del nivel de despegue en la geometría de los sistemas de cabalgamientos: modelos analógicos preliminares. Geotemas (Madrid) (13), 521–524.

Lohrmann, J., Kukowski, N., Adam, J., Oncken, O., 2003. The impact of analogue material properties on the geometry, kinematics, and dynamics of convergent sand wedges. J. Struct. Geol. 25 (10), 1691–1711.

Luján, M., Storti, F., Balanyá, J.C., Crespo-Blanc, A., Rossetti, F., 2003. Role of décollement material with different rheological properties in the structure of the Aljibe thrust imbricate (Flysch Trough, Gibraltar Arc): an analogue modelling approach. J. Struct. Geol. 25 (6), 867–881.

Mandl, G., De Jong, L.N.J., Maltha, A., 1977. Shear zones in granular material: an experimental study of their structure and mechanical genesis. Rock Mech. 9, 95–144.

Marshak, S., 2004. Salients, recesses, arcs, Oroclines, and Syntaxes A review of ideas concerning the formation of map-view curves in fold-thrust belts. In: McClay, K.R. (Ed.), Thrust Tectonics and Hydrocarbon Systems: AAPG Memoir 82, pp. 133–158.

Meigs, A.J., Burbank, D.W., 1997. Growth of the South pyrenean orogenic wedge. Tectonics 16 (2), 239–258.

Milazzo, F., Cavozzi, C., Corti, G., Maestrelli, D., Storti, F., 2021. Centrifuge modelling of thrust systems in the brittle crust: role of frictional décollement geometry. J. Struct. Geol. 153, 104450.

Mochales, T., Barnolas, A., Pueyo, E.L., Serra-Kiel, J., Casas, A.M., Samsó, J.M., et al., 2012. Chronostratigraphy of the Boltaña anticline and the Ainsa basin (southern Pyrenees). GSA Bulletin 124 (7–8), 1229–1250.

Mulugeta, G., 1988. Modelling the geometry of Coulomb thrust wedges. J. Struct. Geol. 10 (8), 847–859.

Muñoz, J.A., 1992. Evolution of a continental collision belt: ECORS-Pyrenees crustal balanced cross-section. In: Thrust Tectonics. Springer, Dordrecht, pp. 235–246.

Muñoz, J.A., Beamud, E., Fernández, O., Arbués, P., Dinarès-Turell, J., Poblet, J., 2013. The Ainsa Fold and thrust oblique zone of the central Pyrenees: kinematics of a curved contractional system from paleomagnetic and structural data. Tectonics 32 (5), 1142–1175.

Reiter, K., Kukowski, N., Ratschbacher, L., 2011. The interaction of two indenters in analogue experiments and implications for curved fold-and-thrust belts. Earth Planet Sci. Lett. 302 (1–2), 132–146.

Rosenbaum, G., Lister, G.S., Duboz, C., 2002. Relative motions of Africa, Iberia and Europe during alpine orogeny. Tectonophysics 359, 117–129.

Santolaria, P., Harris, L.B., Casas, A.M., Soto, R., 2022. Influence of décollement-cover thickness variations in fold-and-thrust belts: insights from centrifuge analog modeling. J. Struct. Geol. 163, 104704.

Schellart, W.P., 2000. Shear test results for cohesion and friction coefficients for different granular materials: scaling implications for their usage in analogue modelling. Tectonophysics 324 (1–2), 1–16.

Schellart, W.P., Strak, V., 2016. A review of analogue modelling of geodynamic processes: approaches, scaling, materials and quantification, with an application to subduction experiments. J. Geodyn. 100, 7–32.

Schreurs, G., et al., 2006. Analogue Benchmarks of Shortening and Extension Experiments, vol. 253. Geological Society, London, Special Publications, pp. 1–27.

Schreurs, G., Hanni, R., Vock, P., Koyi, H.A., Mancktelow, N.S., 2001. Four-dimensional Analysis of Analog Models: Experiments on Transfer Zones in Fold and Thrust Belts. MEMOIRS-GEOLOGICAL SOCIETY OF AMERICA, pp. 179–190.

Soto, R., Storti, F., Casas-Sainz, A.M., 2006. Impact of backstop thickness lateral variations on the tectonic architecture of orogens: insights from sandbox analogue modeling and application to the Pyrenees. Tectonics 25 (2).

Suess, E., 1909. The Face of the Earth: Das Antlitz Der Erde, vol. 4. Clarendon Press.

Tavani, S., Storti, F., Lacombe, O., Corradetti, A., Muñoz, J.A., Mazzoli, S., 2015. A review of deformation pattern templates in foreland basin systems and fold-and-thrust belts: implications for the state of stress in the frontal regions of thrust wedges. Earth Sci. Rev. 141, 82–104.

Teixell, A., 1998. Crustal structure and orogenic material budget in the west central Pyrenees. Tectonics 17, 395–406.

Teixell, A., Koyi, H.A., 2003. Experimental and field study of the effects of lithological contrasts on thrust-related deformation. Tectonics 22 (5).

Van Keken, P.E., Spiers, C.J., Van den Berg, A.P., Muyzert, E.J., 1993. The effective viscosity of rocksalt: implementation of steady-state creep laws in numerical models of salt diapirism. Tectonophysics 225 (4), 457–476.

Vendeville, B.C., Pengcheng, T., Graveleau, F., Shaoying, H., Wang, X., 2017. How the presence of a salt décollement in the sedimentary cover influences the behavior of subsalt thrusts in fold-and-thrust belts. BSGF-Earth Sci. Bull. 188 (6), 37.

Vergés, J., Fernàndez, M., Martìnez, A., 2002. The Pyrenean orogen: pre-, syn-, and post-collisional evolution. J. Virtual Explor. 8, 55–74.

Vidal-Royo, O., Koyi, H.A., Muñoz, J.A., 2009. Formation of orogen-perpendicular thrusts due to mechanical contrasts in the basal décollement in the Central External Sierras (Southern Pyrenees, Spain). J. Struct. Geol. 31 (5), 523–539.

Weil, A.B., Yonkee, A., Sussman, A., 2010. Reconstructing the kinematic evolution of curved mountain belts: a paleomagnetic study of Triassic red beds from the Wyoming salient, Sevier thrust belt, USA. GSA Bulletin 122 (1–2), 3–23.

Weil, A.B., Sussman, A.J., 2004. Classifying curved orogens based on timing relationships between structural development and vertical-axis rotations. In: Orogenic Curvature: Integrating Paleomagnetic And Structural Analyses, 383. Geological Society of America, pp. 1–15.